



# DIGITAL ACCESS TO SCHOLARSHIP AT HARVARD

## Mode-Locked Pulses from Mid-Infrared Quantum Cascade Lasers

The Harvard community has made this article openly available.  
[Please share](#) how this access benefits you. Your story matters.

<b>Citation</b>	Wang, Christine Y., Lyuba Kuznetsova, Gkotsas Vasileios Marios, Laurent Diehl, Franz X. Kaertner, Mikhail A. Belkin, Alexey Belyanin, Xiaofeng Li, Donhee Ham, Harald Schneider, Peter Grant, et al. 2009. Mode-locked pulses from mid-infrared quantum cascade lasers. <i>Optics Express</i> 17(15): 12929-12943.
<b>Published Version</b>	<a href="https://doi.org/10.1364/OE.17.012929">doi:10.1364/OE.17.012929</a>
<b>Accessed</b>	February 18, 2015 4:04:40 AM EST
<b>Citable Link</b>	<a href="http://nrs.harvard.edu/urn-3:HUL.InstRepos:3425949">http://nrs.harvard.edu/urn-3:HUL.InstRepos:3425949</a>
<b>Terms of Use</b>	This article was downloaded from Harvard University's DASH repository, and is made available under the terms and conditions applicable to Other Posted Material, as set forth at <a href="http://nrs.harvard.edu/urn-3:HUL.InstRepos:dash.current.terms-of-use#LAA">http://nrs.harvard.edu/urn-3:HUL.InstRepos:dash.current.terms-of-use#LAA</a>

*(Article begins on next page)*

# Mode-locked pulses from mid-infrared Quantum Cascade Lasers

Christine Y. Wang,<sup>1</sup> Lyuba Kuznetsova,<sup>2</sup> V. M. Gkortsas,<sup>3</sup> L. Diehl<sup>2</sup>, F. X. Kärtner<sup>3</sup>, M. A. Belkin<sup>2</sup>, A. Belyanin<sup>4</sup>, X. Li<sup>2</sup>, D. Ham<sup>2</sup>, H Schneider<sup>5</sup>, P. Grant<sup>6</sup>, C. Y. Song<sup>6</sup>, S. Haffouz<sup>6</sup>, Z. R. Wasilewski<sup>6</sup>, H. C. Liu<sup>6</sup> and Federico Capasso<sup>2,\*</sup>

<sup>1</sup>Department of Physics and <sup>2</sup>School of Engineering and Applied Sciences, Harvard University, Cambridge, MA 02138, USA

<sup>3</sup>Research Laboratory of Electronics, Massachusetts Institute of Technology, Cambridge, MA 02139, USA

<sup>4</sup>Department of Physics, Texas A&M University, College Station, Texas 77843, USA

<sup>5</sup>Institute of Ion Beam Physics and Materials Research, Forschungszentrum Dresden-Rossendorf, 01314, Dresden, Germany

<sup>6</sup>Institute for Microstructural Sciences, National Research Council, Ottawa K1A 0R6, Ontario, Canada

\*[lyuba@seas.harvard.edu](mailto:lyuba@seas.harvard.edu); [capasso@seas.harvard.edu](mailto:capasso@seas.harvard.edu)

**Abstract:** In this study, we report the unequivocal demonstration of mid-infrared mode-locked pulses from quantum cascade lasers. The train of short pulses was generated by actively modulating the current and hence the gain of an edge-emitting quantum cascade laser (QCL). Pulses with duration of about 3 ps at full-width-at-half-maxima and energy of 0.5 pJ were characterized using a second-order interferometric autocorrelation technique based on a nonlinear quantum well infrared photodetector. The mode-locking dynamics in the QCLs was modeled based on the Maxwell-Bloch equations in an open two-level system. Our model reproduces the overall shape of the measured autocorrelation traces and predicts that the short pulses are accompanied by substantial wings as a result of strong spatial hole burning. The range of parameters where short mode-locked pulses can be formed is found.

©2009 Optical Society of America

**OCIS codes:** (140.3070) Infrared and far-infrared lasers; (140.4050) Mode-locked lasers; (140.5965) Semiconductor lasers, quantum cascade

---

## References and links

1. J. J. Macklin, J. D. Kmetec, and C. L. Gordon 3rd, "High-order harmonic generation using intense femtosecond pulses," *Phys. Rev. Lett.* **70**(6), 766–769 (1993).
2. J. M. Dudley, G. Genty, and S. Coen, "Supercontinuum generation in photonic crystal fiber," *Rev. Mod. Phys.* **78**(4), 1135–1184 (2006).
3. E. A. Gibson, A. Paul, N. Wagner, R. Tobey, D. Gaudiosi, S. Backus, I. P. Christov, A. Aquila, E. M. Gullikson, D. T. Attwood, M. M. Murnane, and H. C. Kapteyn, "Coherent soft x-ray generation in the water window with quasi-phase matching," *Science* **302**(5642), 95–98 (2003).
4. R. Huber, F. Tauser, A. Brodschelm, M. Bichler, G. Abstreiter, and A. Leitenstorfer, "How many-particle interactions develop after ultrafast excitation of an electron-hole plasma," *Nature* **414**(6861), 286–289 (2001).
5. R. Torre, P. Bartolini, and R. Righini, "Structural relaxation in supercooled water by time-resolved spectroscopy," *Nature* **428**(6980), 296–299 (2004).
6. D. Meshulach, and Y. Silberberg, "Coherent quantum control of two-photon transitions by a femtosecond laser pulse," *Nature* **396**(6708), 239–242 (1998).
7. W. S. Warren, H. Rabitz, and M. Dahleh, "Coherent Control of Quantum Dynamics: The Dream Is Alive," *Science* **259**(5101), 1581–1589 (1993).
8. T. Udem, R. Holzwarth, and T. W. Hänsch, "Optical frequency metrology," *Nature* **416**(6877), 233–237 (2002).

9. P. Loza-Alvarez, C. T. Brown, D. T. Reid, W. Sibbett, and M. Missey, "High-repetition-rate ultrashort-pulse optical parametric oscillator continuously tunable from 2.8 to 6.8  $\mu\text{m}$ ," *Opt. Lett.* **24**(21), 1523–1525 (1999).
10. S. French, M. Ebrahimzadeh, and A. Miller, "High-power, high-repetition-rate picosecond optical parametric oscillators for the near- to mid-infrared," *J. Mod. Opt.* **43**, 929–952 (1996).
11. M. R. X. de Barros, R. S. Miranda, T. M. Jedju, and P. C. Becker, "High-Repetition-Rate Femtosecond Midinfrared Pulse Generation," *Opt. Lett.* **20**(5), 480–482 (1995).
12. H. Okamoto, and M. Tasumi, "Generation of Ultrashort Light-Pulses in the Midinfrared (3000–800  $\text{cm}^{-1}$ ) by 4-Wave-Mixing," *Opt. Commun.* **121**(1–3), 63–68 (1995).
13. J. Faist, F. Capasso, D. L. Sivco, C. Sirtori, A. L. Hutchinson, and A. Y. Cho, "Quantum Cascade Laser," *Science* **264**(5158), 553–556 (1994).
14. C. Gmachl, D. L. Sivco, R. Colombelli, F. Capasso, and A. Y. Cho, "Ultra-broadband semiconductor laser," *Nature* **415**(6874), 883–887 (2002).
15. C. Y. Wang, L. Diehl, A. Gordon, C. Jirauschek, F. X. Kärtner, A. Belyanin, D. Bour, S. Corzine, G. Höfler, M. Troccoli, J. Faist, and F. Capasso, "Coherent instabilities in a semiconductor laser with fast gain recovery," *Phys. Rev. A* **75**(3), 031802 (2007).
16. A. Gordon, C. Y. Wang, L. Diehl, F. X. Kärtner, A. Belyanin, D. Bour, S. Corzine, G. Höfler, H. C. Liu, H. Schneider, T. Maier, M. Troccoli, J. Faist, and F. Capasso, "Multimode regimes in quantum cascade lasers: From coherent instabilities to spatial hole burning," *Phys. Rev. A* **77**(5), 053804 (2008).
17. H. Choi, T. B. Norris, T. Gresch, M. Giovannini, J. Faist, L. Diehl, and F. Capasso, "Femtosecond dynamics of resonant tunneling and superlattice relaxation in quantum cascade lasers," *Appl. Phys. Lett.* **92**(12), 122114–122117 (2008).
18. H. A. Haus, "Mode-locking of lasers," *IEEE J. Sel. Top. Quantum Electron.* **6**(6), 1173–1185 (2000).
19. F. Capasso, J. Faist, C. Sirtori, D. L. Sivco, A. L. Hutchinson, and A. Y. Cho, "Laser action by tuning the oscillator strength," *Nature* **387**(6635), 777–782 (1997).
20. H. Choi, L. Diehl, Z. K. Wu, M. Giovannini, J. Faist, F. Capasso, and T. B. Norris, "Gain recovery dynamics and photon-driven transport in quantum cascade lasers," *Phys. Rev. Lett.* **100**(16), 167401 (2008).
21. R. Paiella, F. Capasso, C. Gmachl, D. L. Sivco, J. N. Baillargeon, A. L. Hutchinson, A. Y. Cho, and H. C. Liu, "Self-mode-locking of quantum cascade lasers with giant ultrafast optical nonlinearities," *Science* **290**(5497), 1739–1742 (2000).
22. R. Paiella, F. Capasso, C. Gmachl, H. Y. Hwang, D. L. Sivco, A. L. Hutchinson, A. Y. Cho, and H. C. Liu, "Monolithic active mode locking of quantum cascade lasers," *Appl. Phys. Lett.* **77**(2), 169–171 (2000).
23. A. Soibel, F. Capasso, C. Gmachl, M. L. Peabody, A. M. Sergent, R. Paiella, D. L. Sivco; A. Y. Cho; H. C. Liu, "Stability of pulse emission and enhancement of intracavity second-harmonic generation in self-mode-locked quantum cascade lasers," *IEEE J. Quantum Electron.* **40**(3), 197–204 (2004).
24. J.-C. Diels, and W. Rudolph, *Ultrashort laser pulse phenomena: fundamentals, techniques, and applications on a femtosecond time scale* (Academic Press, Boston, 2nd ed. 2006)
25. H. C. Liu, and E. Dupont, "Nonlinear quantum well infrared photodetector," *J. Nonlinear Opt. Phys. Mater.* **11**(4), 433–443 (2002).
26. T. Maier, H. Schneider, H. Liu, M. Walther, and P. Koidl, "Two-photon QWIPs for quadratic detection of weak mid-infrared laser pulses," *Infrared Phys. Technol.* **47**(1–2), 182–187 (2005).
27. P. D. Grant, R. Dudek, M. Buchanan, L. Wolfson, and H. Liu, "An ultra fast quantum well infrared photodetector," *Infrared Phys. Technol.* **47**(1–2), 144–152 (2005).
28. S. Barbieri, W. Mainault, S. S. Dhillon, C. Sirtori, J. Alton, N. Breuil, H. E. Beere, and D. A. Ritchie, "13 GHz direct modulation of terahertz quantum cascade lasers," *Appl. Phys. Lett.* **91**(14), 143510 (2007).
29. H. C. Liu, Jianmeng Li, M. Buchanan, and Z. R. Wasilewski, "High-frequency quantum-well infrared photodetectors measured by microwave-rectification technique," *IEEE J. Quantum Electron.* **32**(6), 1024–1028 (1996).

## 1. Introduction

Stable trains of ultrashort light pulses with large instantaneous intensities from mode-locked lasers are key elements for many important applications such as nonlinear frequency conversion [1–3], time-resolved measurements [4, 5], coherent control [6, 7], and frequency combs [8]. To date, the most common approach to generate short pulses in the mid-infrared (3.5–20  $\mu\text{m}$ ) molecular "fingerprint" region relies on the down-conversion of short-wavelength mode-locked lasers through nonlinear processes, such as optical parametric

generation [9-11] and four-wave mixing [12]. These systems are usually bulky, expensive and typically require a complicated optical arrangement.

Quantum cascade lasers (QCLs) [13], since their invention in 1994, have become the most prominent coherent light sources in the mid-infrared. One of the most striking differences between these unipolar devices and diode lasers is that their emission wavelength, gain spectrum [14], carrier transport characteristics, and optical dispersion can be engineered. This remarkable design freedom makes QCLs a unique candidate to serve as a semiconductor source of ultra-short pulses in the mid-infrared.

There is, however, an obstacle of fundamental origin that has so far prevented achieving ultrashort pulse generation in QCLs [15, 16]. In intersubband transitions, the carrier relaxation is extremely fast because of optical phonon scattering. As a result, the gain recovery time in QCLs, determined both by upper state lifetime and by the electron transport through the cascade heterostructure, is typically on the order of a few picoseconds [17] which is an order of magnitude smaller than the cavity roundtrip time of 40-60 ps for a typical 2-3mm-long laser cavity.

According to conventional mode-locking theory, this situation prevents the occurrence of stable passive mode-locking and impedes the formation of high-intensity pulses through active mode-locking [18]. This can be understood as follows: If the gain recovery time is longer than the cavity roundtrip time, then a single laser pulse oscillating in the cavity depletes the gain and prevents the formation of other pulses; if the gain recovery is much shorter than the cavity roundtrip time, multiple pulses can propagate in the laser cavity, separated, approximately, by the gain recovery time. Finally, if the gain recovery is very fast, faster than the pulse duration, the gain reacts nearly instantaneously on the intensity of the pulse. In this case, the peak of the pulse saturates the gain, and the wings of the pulse, which have too low intensity to saturate the gain, see more gain than the peak of the pulse. This process leads to lengthening of the pulse, i.e. the suppression of intensity fluctuation, which suppresses mode-locking and leads to continuous-wave (CW) lasing. The latter situation is the case in most QCLs.

In this work, we achieve mode-locking by designing a QCL structure with longer phonon-assisted intersubband relaxation time than conventional QCL designs and by actively modulating the pumping current of a short section at one end of the laser cavity to provide net gain to the pulse. Our QCL structure, shown in Figure 1, is based on a "diagonal transition" in real space [19], i.e. the laser transition takes place between levels confined in two adjacent wells separated by a thick barrier. The reduced wavefunction overlap between the upper and lower laser states results in a phonon-limited upper state lifetime of approximately 50 ps below threshold.

In general, the gain recovery in QCL's based on "diagonal transition" has a complex dynamics [20]. The gain recovery is defined by time-dependent transport through both active region and injector. The most important difference from the conventional lasers is that the gain recovery in QCLs has an important component, the transport delay between active regions in the cascade structure. The lasing transition (wave arrow in Fig.1) is between the upper state and the lower state in the active region, which is emptied via tunneling into the injector region. Well below threshold, the upper state lifetime is essentially the phonon-assisted intersubband relaxation time. As the laser approaches and exceeds threshold, the gain recovery is determined almost entirely by lower state emptying and superlattice transport components. So the gain recovery time above the threshold is reduced dramatically to few picoseconds [20]. This speed-up of the gain recovery time makes it hard to achieve mode-locking and prevents stable pulse formation.

As we will see later, in this work we are able to identify a parameter range close to the laser threshold where we can form mode-locked pulses by modulating the gain in the short section of a device. High above threshold, pulses are broadened by the increased gain

saturation in the un-modulated long section, and finally become unstable due to the increased spatial hole-burning and reduced gain recovery time.

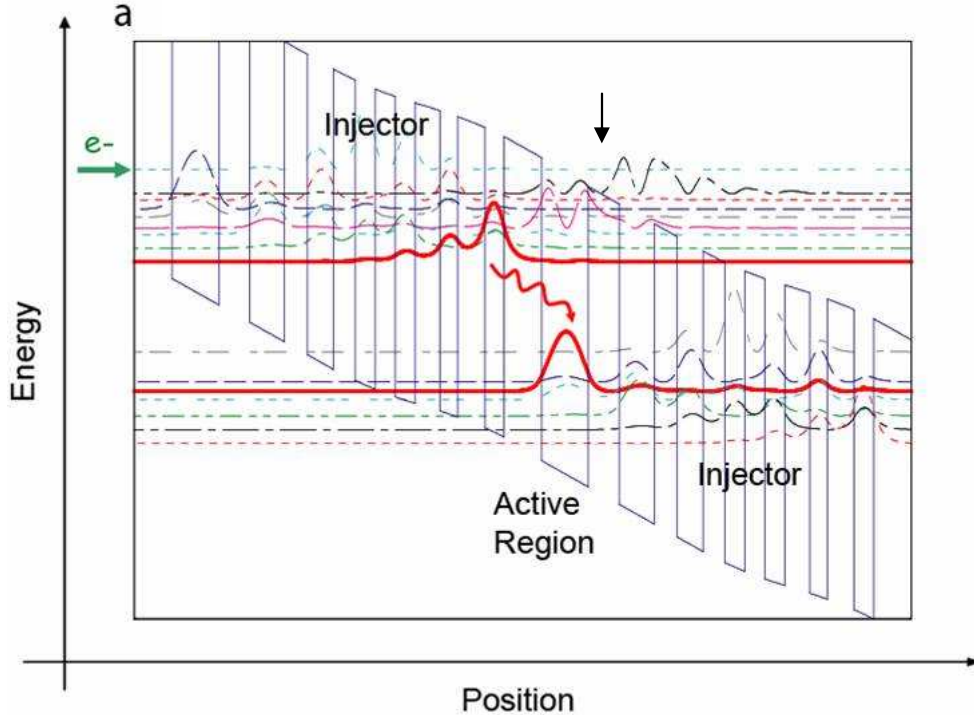


Fig. 1. Calculated conduction band structure of the QCL. The plot represents the potential profile along the growth direction, and the moduli squared of the wavefunctions. The states involved in the laser transition are shown as solid red curves. The barriers (conduction bandoffset = 0.52 eV) are made of  $\text{Al}_{0.48}\text{In}_{0.52}\text{As}$  and the quantum wells of  $\text{Ga}_{0.47}\text{In}_{0.53}\text{As}$  (the barrier is indicated by vertical arrow). The layer thicknesses are (starting from the left, from the injection barrier, in nm): **3.8**/4.7/**3.1**/3.5/**2.3**/2.6/**2.2**/2.0/**2.0**/2.0/**2.5**/1.8/**2.7**/1.9/**3.8**, where the barriers are indicated in boldface and the underlined layers are doped to  $n = 6 \times 10^{17} \text{ cm}^{-3}$ .

There were several reports of mode-locking in QCLs [21-23], whose evidence were based on broadband optical spectra with a large number of longitudinal modes and a narrow microwave beat note in the power spectrum at the laser roundtrip frequency, which indicated that the electric field waveform circulating in the laser cavity and thus the phase relationship between the longitudinal modes was stable over a large number of round-trips. However, due to the lack of a suitable apparatus for second-order autocorrelation measurements, no direct evidence was given to demonstrate that the circulating waveform was indeed a periodic sequence of isolated pulses, which would result from all modes having equal and stable phases. Subsequent pulse characterization using autocorrelation techniques showed that under the previous conditions, the output of free running QCLs was not composed of one isolated pulse per roundtrip [15, 16]. The physics of multimode behaviour observed in those lasers is described by spatial hole-burning and the Risken-Nummedal-Graham-Haken (RNGH) instability [15, 16], rather than by mode locking.

## 2. QCL device processing and characteristics

### 2.1 Device processing and assembling

Our devices were processed into ridge waveguides with multiple electrically independent sections; see Fig. 2 for the diagram of the QCL. The wafer was processed into 2.6 mm long,

8-20  $\mu\text{m}$  wide ridge waveguides by reactive ion etching. A 5  $\mu\text{m}$ -thick layer of Microchem SU-8 2005 photoresist was used as an insulation layer between the wafer and the top contact to reduce the parasitic capacitance. The SU-8 2005 photoresist on top of the ridges was removed by standard photolithography and a metal layer (Ti/Au; 20 nm/300 nm) was then deposited to provide electrical contact. The top Ti/Au contact and the underlying heavily doped InP contact layers were etched out in specific areas along the ridges to create multiple electrically independent sections with minimal electrical crosstalk. A non-alloyed Ge/Au contact was deposited on the back. The samples were indium-soldered on copper holders and mounted in a liquid-nitrogen flow cryostat. The short 120  $\mu\text{m}$  to 160  $\mu\text{m}$ -long section was aluminum-wire-bonded to a gold microstrip connected to an end launch connector and SMA cables for radio frequency (RF) signal injection via a bias tee to modulate the pumping current, while the rest of the ridge was bonded to a regular gold bonding pad.

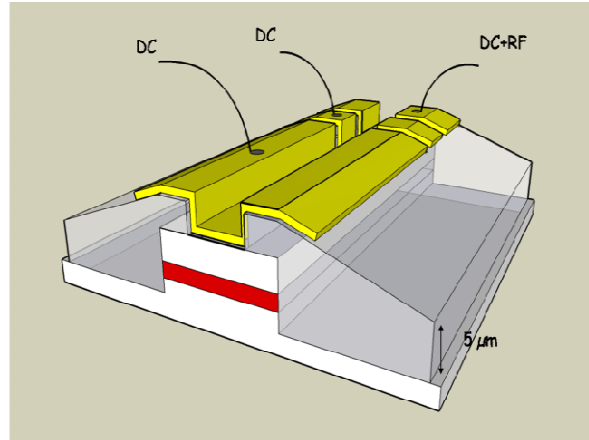


Fig. 2. Diagram of the multi-section QCL, showing the dry-etched laser ridges in white (with active region in red), the 5  $\mu\text{m}$ -thick SU-8 insulating layer in grey, and the gold top contact in yellow. The top metal contact layer and the underlying heavily doped region grown above the top cladding layer are disconnected between the sections. The whole 2.6 mm-long laser is biased under the same DC voltage, while a RF modulation is added to the short section (120-160 $\mu\text{m}$ ) at the end of the ridge.

## 2.2 QCL characteristics

The current-voltage (I-V) and light-current (L-I) characteristics of a 16 $\mu\text{m}$ -wide ridge device when the whole ridge is pumped in continuous wave (CW) with no RF modulation at 77K are shown in Figure 3. The CW threshold current is 310 mA, which gives a threshold current density of 0.745 kA/cm<sup>2</sup>. The maximum CW operating temperature of this structure is about 200 K. The differential resistance of the RF section above threshold is  $R \approx 30 \Omega$ . Given the estimated capacitance across the insulation layer  $C \approx 0.05 \text{ pF}$ , the RC-limited frequency response extends to  $\sim 100 \text{ GHz}$ , far above the roundtrip frequency of the laser cavity. The actual microwave power delivered to the device measured by a network analyzer was about 30% of the input power, which indicates a significant impedance mismatch between the source and the device. The largest contribution to the impedance mismatch is the inductance caused by the bond wire, estimated to be about 1 nH (see Appendix).

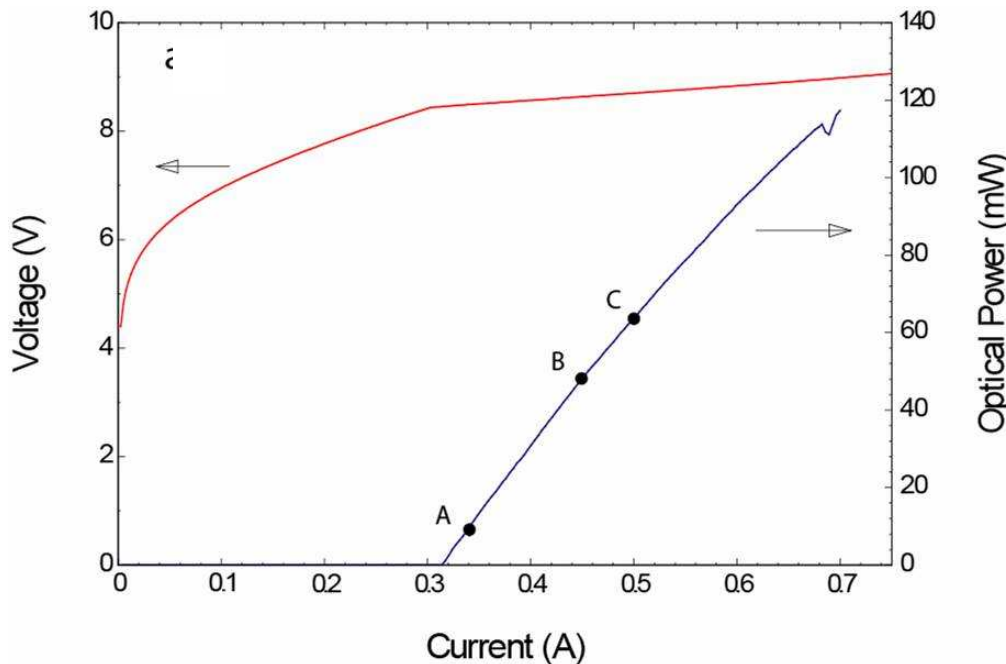


Fig. 3. The current-voltage (I-V) and output power-current (L-I) characteristics of the 16  $\mu\text{m}$  wide QCL with no RF modulation. The laser threshold is at 310 mA. A, B, C denote the currents ( $I=340$  mA, 450 mA & 500mA) at which currents the pulse characterization was performed.

Figure 4a shows the optical spectra of the device, measured with a Fourier transform infrared spectrometer (FTIR) equipped with a deuterated triglycine sulphate (DTGS) detector, as a function of the RF modulation frequency, for a DC pumping current of 340 mA which is about 1.1 times the laser threshold. The RF input power was kept constant at 35 dBm. The laser emission is single mode when no gain modulation is applied. At a gain modulation frequency corresponding to the laser roundtrip frequency of 17.86 GHz we observe significant spectral broadening. The spectrum exhibits many longitudinal modes with an approximately Gaussian envelope. With a slightly detuned RF frequency from resonance, the laser spectrum becomes narrower. When the RF frequency is tuned further away from resonance ( $<17.36$  GHz or  $>18.11$  GHz), lasing stops. The RF power is able to suppress the lasing up to 355 mA of pumping current. As we shall see, isolated mode-locked pulses are formed for pumping close to threshold; gain can overcome loss only if the RF frequency is tuned to resonance, and the laser generates a train of isolated short pulses which reach the modulated section at each round-trip at its gain maximum. When the laser is pumped at higher DC current (1.45 times the laser threshold), the optical spectra show similar resonance behaviour, but the RF modulation is no longer sufficiently strong to suppress the lasing when the detuning between the RF modulation frequency and the cavity round-trip frequency is large (Fig. 4b).

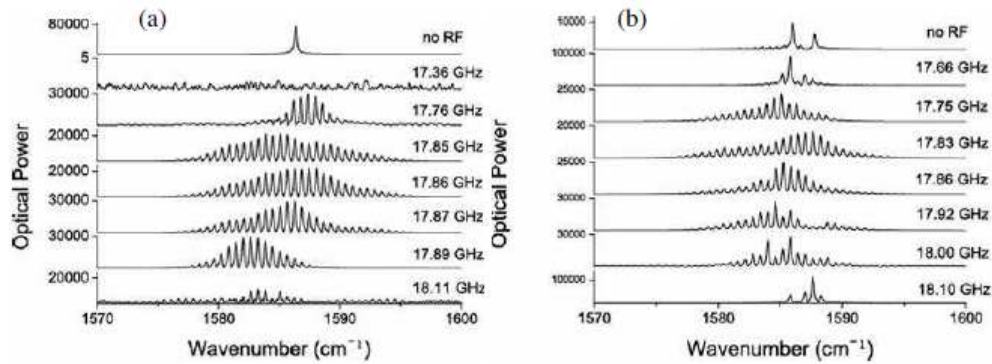


Fig. 4. (a) Spectra of the QCL at 340 mA and (b) at 450 mA with 35 dBm of input RF modulation at various modulation frequencies. Note that the scales of the optical power of the spectra are different at 340 mA. All measurements were performed at a heat sink temperature of  $T=77\text{K}$ .

### 3. Pulse characterization

#### 3.1 Second-order interferometric autocorrelation

The laser emission is characterized using a second-order interferometric autocorrelation (IAC) technique [16, 24] using a two-photon quantum well infrared photodetector (QWIP) [25, 26]. The IAC measurement was based on a Michelson interferometer (Fig. 5). The laser beam first passed through a chopper, and was then sent to a Ge beam splitter with antireflection coating on one side. The transmitted and reflected beams were then sent into two broadband retroreflectors coated with gold, with one of the retroreflectors mounted on a stepping motor. Once recombined by the beam splitter, the two beams were sent collinearly to a two-photon QWIP with operating wavelength centred at  $6.2\ \mu\text{m}$ . The resulting photocurrent was then sent to a current pre-amplifier, followed by a lock-in amplifier whose reference frequency was determined by the chopper. The signal from the lock-in amplifier was recorded by a computer which controls the stepper motor simultaneously. For the case of isolated periodic pulses, the ratio between the interference maximum and the background should be 8 to 1 [16].

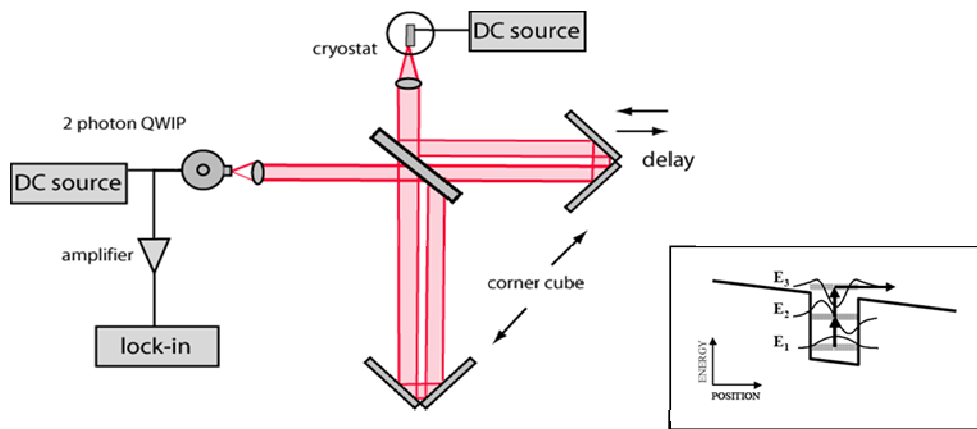


Fig. 5. The experimental setup for the autocorrelation measurement using two-photon QWIP. Inset: conduction band diagram of the two-photon QWIP showing three equidistant energy levels.



### 3.1.1 Varying DC pumping (fixed RF power)

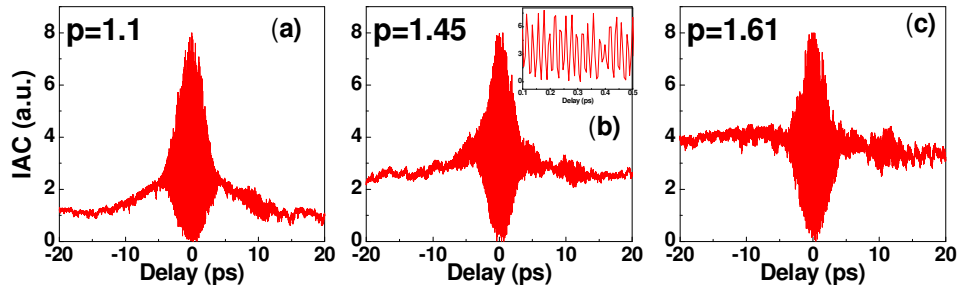


Fig. 6. Interferometric autocorrelation traces (IACs) of the 16  $\mu\text{m}$ -wide QCL output with 35 dBm of applied modulation at (a) 340 mA (1.1 times the laser threshold), (b) 450 mA (1.45 times the laser threshold) and (c) 500 mA (1.61 times the laser threshold), respectively. Inset (b): detail of the interference fringes from 0.1 ps to 0.5 ps. All measurements were performed at a heat sink temperature of  $T=77\text{K}$  and RF modulation frequency at 17.86 GHz.

Figure 6a shows the IAC trace obtained when the 16  $\mu\text{m}$ -wide QCL is DC-pumped at 340 mA and the RF modulation of 35 dBm is applied at the cavity resonance frequency of 17.86 GHz. The observed peak-to-background ratio is 8:1, indicating mode-locking and the circulation of an isolated pulse per roundtrip in the cavity. The full-width-at-half-maximum (FWHM) pulse duration, estimated from the width of the interference fringes, is  $\sim 3$  ps. The FWHM pulse duration is approximately a factor of two larger than the width of a Fourier-transform limited pulse duration calculated from the optical spectrum in Fig. 4a. The pulse has extended wings up to  $\sim 10$  ps, indicating a complicated phase profile. The estimated energy per pulse is close to 0.5 pJ. The replication of the IAC trace over two roundtrips was verified.

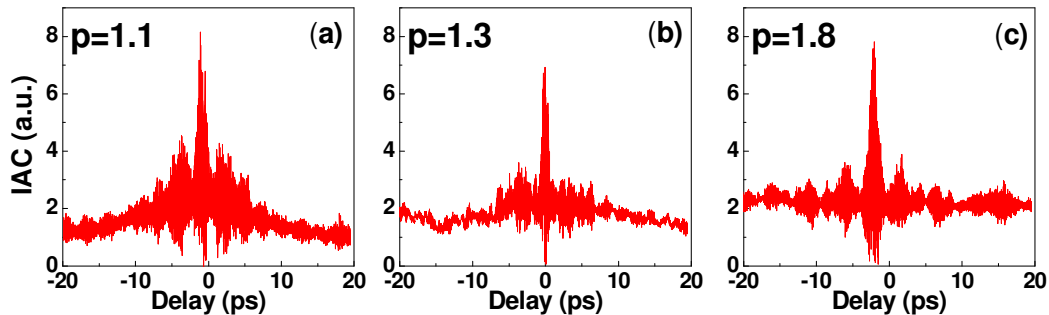


Fig. 7. Interferometric autocorrelation traces (IACs) of the 12  $\mu\text{m}$ -wide QCL output with 35 dBm of applied modulation at (a) 265 mA (1.08 times the laser threshold), (b) 323 mA (1.32 times the laser threshold) and (c) 450 mA (1.84 times the laser threshold), respectively. All measurements were performed at a heat sink temperature of  $T=77\text{K}$  and RF modulation frequency at 17.415 GHz.

When the DC pumping is increased to 450 mA, the peak-to-background ratio of the IAC is no longer 8:1, but rather 8:2.5, as shown in Fig. 6b. This indicates that the laser output does no longer consist of isolated pulses separated by the roundtrip time, but rather of overlapping pulses with an incoherent background. Further increasing the laser pumping current to 500 mA with fixed RF power decreases the peak-to-background ratio of the IAC even more to 8:4, see Fig. 6c.

Similar trend is observed for the 12  $\mu\text{m}$ -wide QCL (Fig. 7). The peak-to-background ratio of the IAC gradually decreases with higher DC pumping current.

### 3.1.2 Varying RF power (fixed DC pumping)

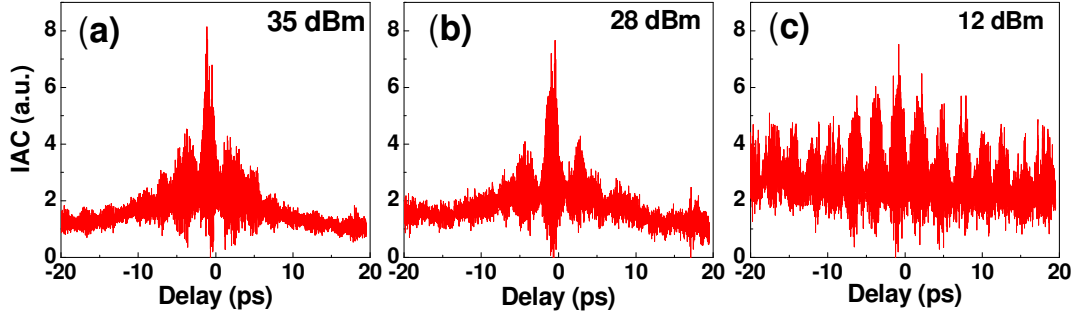


Fig. 8. Interferometric autocorrelation traces (IACs) of the 12  $\mu\text{m}$ -wide QCL output at 265 mA (1.08 times the laser threshold) with (a) 35 dBm, (b) 28 dBm & (c) 12 dBm of RF input powers, respectively. All measurements were performed at a heat sink temperature of  $T=77$  K and RF modulation frequency at 17.415 GHz.

Figures 8a-c show the IAC for a 12  $\mu\text{m}$ -wide laser with various RF power levels when the laser was pumped at 265 mA (about 1.08 times the laser threshold). The pulse quality degrades dramatically as the RF input power decreases from 35 dBm to 12 dBm. Thus, operating near threshold and applying sufficiently large RF modulation are two necessary conditions to achieve stable mode-locking in our devices. For fixed input RF power (35 dBm) the IAC shows a similar behavior to that of the 16  $\mu\text{m}$  wide device as the DC pumping is increased.

### 3.2 Microwave spectrum

The microwave spectrum of the laser output was measured with a fast QWIP. The laser output was focused directly onto the fast QWIP, and the resulting photocurrent was displayed on a spectrum analyzer. The resolution bandwidth of the spectrum analyzer was 330 Hz for the measurement.

The microwave spectrum of the 16- $\mu\text{m}$ -wide laser output at DC pumping of 340 mA with 35 dBm of applied RF modulation is shown in Fig. 9. A narrow peak with a FWHM of  $\sim 3$  kHz was observed at the RF modulation frequency, which indicates phase coherence between the modes for more than  $10^6$  roundtrips. This beat note is also at least an order of magnitude narrower than any previously observed beat note from multimode QCLs [23]. Increasing the DC pumping current does not result in any observable increase of the signal width, although IAC measurements show that single-pulse mode locking gets destroyed in this case. Therefore, the previously observed sharp beat note cannot by itself constitute the proof of a mode-locking.

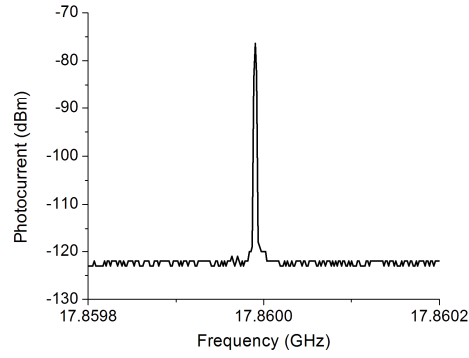


Fig. 9. Microwave spectrum of photocurrent generated by the 16  $\mu\text{m}$ -wide laser pumped at 340 mA with 35 dBm of applied RF modulation.

#### 4. Modeling

Modulating the injection current of the QCLs leads to modulation of the gain. In that case, the standard active mode-locking formalism of loss modulation which does not take the gain dynamics into account cannot be applied [18]. To understand the pulse regimes in our system, we use a simplified model based on one-dimensional Maxwell-Bloch equations in a Fabry-Perot cavity, where the active medium is described by an open two-level system. This model has been shown to successfully describe the dynamics in our previous experiments using QCLs without active modulation [15, 16].

##### 4.1 Maxwell-Bloch equations

The QCL gain structure is modelled as an open two-level system described by optical Bloch equations and the pulse propagation through the gain medium in the Fabry-Perot cavity is described by a one-dimensional wave equation. In the slowly varying envelope approximation, the equations read [1]

$$\partial_t \eta_{\pm} = \frac{i}{2} (\Delta_0 \varepsilon_{\pm} + \Delta_2^* \varepsilon_{\mp}) - \frac{\eta_{\pm}}{T_2} \quad (1)$$

$$\partial_t \Delta_0 = \lambda + i(\varepsilon_+^* \eta_+ - \eta_+^* \varepsilon_+ + \varepsilon_-^* \eta_- - \eta_-^* \varepsilon_-) - \frac{\Delta_0}{T_1} \quad (2)$$

$$\partial_t \Delta_2 = i(-\eta_+^* \varepsilon_- + \varepsilon_+^* \eta_-) - \frac{\Delta_2}{T_1} - 4k^2 D \Delta_2 \quad (3)$$

$$\left( \pm \partial_z + \frac{n}{c} \partial_t \right) \varepsilon_{\pm} = -\frac{i\omega N d^2}{\hbar \varepsilon_0 c n} \eta_{\pm} - l \varepsilon_{\pm} \quad (4)$$

where  $k \equiv n\omega/c$ . The + and - subscripts label the two directions of propagation.  $\varepsilon$  and  $\eta$  are the slowly varying envelopes of the electric field and the polarization, respectively. The actual electric field and polarization are obtained by multiplying  $\varepsilon_{\pm}$  and  $\eta_{\pm}$  by  $e^{i(\pm\omega t - kz)}$  ( $\omega$  is the optical frequency) and taking the real part. The population inversion  $\Delta$  is decomposed into  $\Delta(z, t) = \Delta_0(z, t) + \Delta_2(z, t) e^{2ikz} + \Delta_2^*(z, t) e^{-2ikz}$ , where  $\Delta_0$  is the average inversion and  $\Delta_2$  the strength of the inversion grating allowing spatial hole burning to be taken into account.

Both quantities are also assumed to vary slowly in time and space.  $D$  is the diffusion coefficient of the inversion grating ( $D=46 \text{ cm}^2/\text{s}$  at 77 K). The lifetime of the inversion grating

is given as  $T_g^{-1} = T_1^{-1} + 4k^2D$ , where  $k$  is the wavenumber at the centre wavelength of the QCL  $k = 1.013 \times 10^6 \text{ m}^{-1}$ .  $N$  is the number of two-level systems per unit volume,  $d$  is the dipole matrix element of the laser transition,  $n$  is the refractive index,  $l$  represents the linear losses,  $\lambda$  is the pumping rate, and  $T_1$  and  $T_2$  are the longitudinal and transverse relaxation times, respectively. We assume the parameters  $T_1 = 50 \text{ ps}$ ,  $T_2 = 50 \text{ fs}$  (corresponding to a gain FWHM bandwidth of  $27 \text{ meV}$ ),  $l = 10 \text{ cm}^{-1}$ , and  $n = 3.2$ .

The cavity is  $2.6 \text{ mm}$  long and has a short electrically isolated section at one end of the cavity. Physically the short section is  $120\text{-}160 \text{ }\mu\text{m}$  long, however, due to imperfect electrical isolation between the long and the short sections, the RF power spreads from the short into the long section. Taking the current spreading into account, effectively we are modulating an area almost twice as big as the actual short section (see Appendix). Thus in the modelling we use  $240 \text{ }\mu\text{m}$  for the length of the short section. The short section and the rest of the waveguide are equally DC pumped at  $\lambda = p \times \lambda_{th}$ , where  $\lambda_{th}$  denotes the pumping at threshold, and  $p$  the pumping ratio. At the short section, we assume an additional sinusoidal modulation to the pumping:  $\lambda = \lambda_{th} \times [p + m \sin(2\pi f_R t)]$ , where  $m$  is the modulation amplitude, and  $f_R$  is the cavity roundtrip frequency. The modulation amplitude is estimated to be about 5 for  $35 \text{ dBm}$  RF power (see Appendix).

#### 4.2 Simulation results

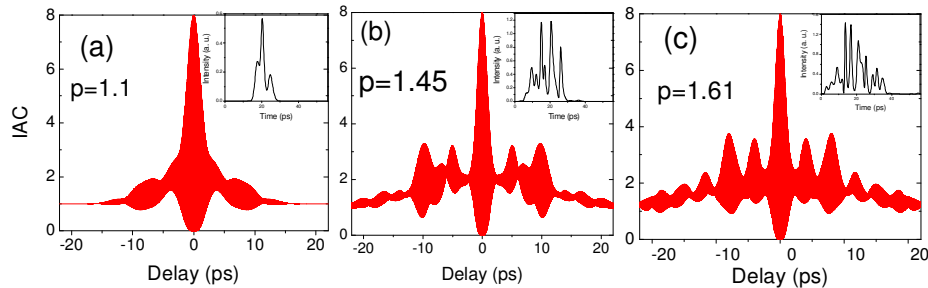


Fig. 10. Simulated interferometric autocorrelation traces (IACs) at (a)  $p=1.1$ , (b)  $p=1.45$ , and (c)  $p=1.61$ , with fixed modulation amplitude  $m=5$ . Insets show the corresponding intensity profile of one round-trip.

Figures 10a-c shows the simulated IACs for fixed modulation amplitude  $m=5$  with different pumping ratios  $p$  corresponding to the experimental pumping ratios in Fig. 6, and Fig. 11a-c show the simulated IACs for fixed pumping ratio  $p=1.1$  with different modulation amplitudes  $m$  corresponding to the estimated experimental modulation amplitudes in Fig. 8. For  $p=1.1$  and  $m=5$ , the peak-to-background ratio of the IAC is 8:1, and the ratio gradually decreases with higher DC pumping  $p$  and smaller modulation amplitude  $m$ , which follows the experimental trend. Note however that there remain quantitative discrepancies with experiments, which show a faster decrease of the IAC ratio with increasing  $p$  and decreasing  $m$ . One reason for the discrepancy could be a faster gain recovery time than  $T_1 = 50 \text{ ps}$  assumed in the modelling. Gain recovery is expected to have not only a component determined by the phonon-assisted intersubband relaxation time, but also a component determined by electron transport between the injector and the active region, with a characteristic time scale of a few ps [20]. The simplified two-level model effectively neglects

the superlattice transport. Our modelling does show rapid deterioration of stable mode locking with decreasing  $T_1$ . To predict the exact level of the IAC background, for a given pumping and modulation conditions, a simple two-level mode used here is not sufficient and a more detailed description of the laser gain as a function of pumping conditions and laser operation is needed [20].

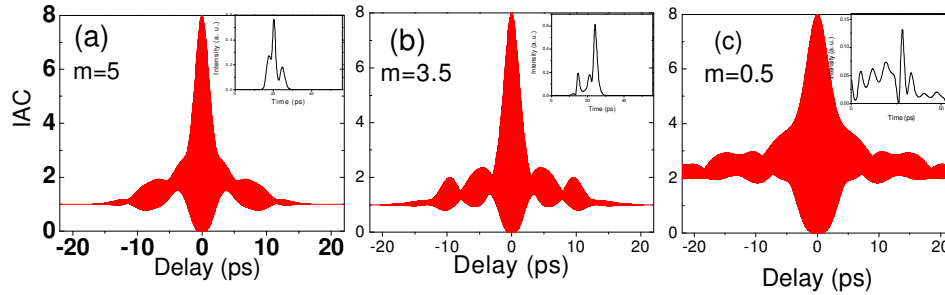


Fig. 11. Simulated IACs with modulation amplitude (a)  $m=5$ , (b)  $m=3.5$  and (c)  $m=0.5$ , respectively, with fixed DC pumping  $p=1.1$ . The insets show the corresponding intensity profile of one round-trip.

In both experiment and simulation, we observe side lobes in the IACs beside the main interference peak. The side lobes in the simulations come from the multiple spikes in the intensity profile, as seen in the insets of Fig. 10a-c and Fig. 11a-c. These spikes indicated that the phase of the pulse has complicated shape. The most likely cause for these spikes is spatial hole-burning (SHB) in the laser gain created by standing waves in the cavity. The gain grating introduced by SHB interferes with active mode locking as it couples the longitudinal modes and reduces the phase locking imposed by the gain modulator. As a result, the modes develop nonlinear phases that lead to a waveform with multiple spikes. Note that in the experimental IACs, the 12  $\mu\text{m}$ -wide device (Fig. 7) has more pronounced lobes than the 16  $\mu\text{m}$ -wide one (Fig. 6). This is consistent with our previous observation that SHB is less significant in wider devices because multiple transverse modes tend to wash out the gain grating formed by SHB [16].

In general, it was found in numerical simulations that strong SHB reduces the FWHM pulse duration in the expense of pulse stability. SHB is strong enough to enable multimode lasing in CW regime for relatively modest pumping ratio  $p > 1.1$ . Strong SHB also results in incomplete mode locking for high pumping ratio even when the sufficiently large modulation is applied (Fig. 8. c).

## 5. Conclusion

We have demonstrated the first unequivocal mode-locking in QCLs via active gain modulation. As revealed by the IAC, isolated periodic pulses with FWHM as short as 3 ps can be generated in the vicinity of the laser threshold. The presence of non-negligible wings is evident in the measured IAC traces and is predicted by our model as a result of strong spatial hole burning. Experimental data and numerical simulations show that the parameter window for stable mode-locking is determined by both the DC pumping current and the RF modulation power. Numerical simulations predict that the peak-to-background ratio of the IAC gradually decreases with higher DC pumping  $p$  and smaller modulation amplitude  $m$ , which follows the experimental trend. Further pulse shortening can be achieved by

incorporating saturable absorber or increasing gain lifetime. We anticipate our results to be a significant step toward a compact, electrically-pumped source generating ultrashort light pulses in the mid-infrared and terahertz spectral ranges.

## 6. Appendix

### 6.1 Estimation of current spreading

For active mode locking in QCLs, we send a RF signal into a short section (160 $\mu\text{m}$  long) at the end of the laser ridge (2.6mm long). The schematic is shown in Fig. 2.

Although the top metal contact and the underlying highly doped layer are etched between the sections, there is still electrical cross talk. To estimate how much current spreads from the short section into the long section, we measured the DC current-voltage (I-V) characteristics of the short section both when the long section is floating and biased at the laser threshold voltage of 8V, and compare them with the I-V curve of the whole laser with current scaled down by the ratio of the whole laser length to the short section length, i.e., 2.6mm/160 $\mu\text{m}$ =16.25. The result from a 12 $\mu\text{m}$ -wide ridge laser is shown below:

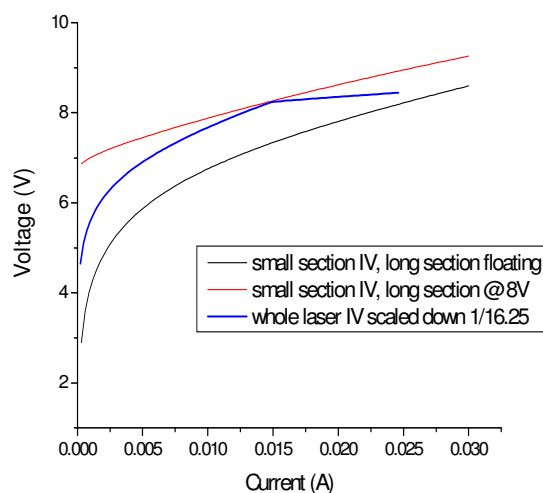


Fig. 12. DC I-V characteristics of the small section when the long section is float (black curve), biased at 8V (red curve), and the whole laser I-V scaled down 1/16.25.

If there is no current spreading between the short and long sections, since they are pumped in parallel, the short section I-V should overlap with the blue curve below threshold. At the threshold voltage 8V, the red and blue curves coincide. This agrees with what we would expect, since when both long and short sections are pumped at the same voltage, there is effectively no current spreading. However, at 8V the current value of the black curve is about twice the current value of the red and blue curves. This indicates that current spreads over an area about twice the short section area. So the RF signal is effectively modulating an area twice as big as the short section area, and the modulation amplitude is about half as big as if there is no current spreading.

### 6.2 Simulation of RF current

The equivalent circuit representing the major parasitic elements in the devices tested in this paper is shown in Fig. 13. The circuit diagram is similar to that used for other high-frequency devices, see, e.g., Refs. [28, 29]:

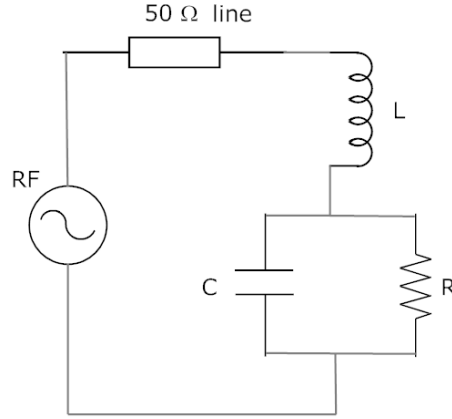


Fig. 13. Equivalent circuit of a packaged device. The QCL is mounted at the end of a 50-Ω transmission line. The QCL is modeled by a parallel resistance-capacitance equivalent circuit, and the parasitic inductance is caused by the short bonding wire connecting the line to the laser.

The inductance element in Fig. 13 is caused by the bonding wire and the capacitance element is caused by the capacitance between the top and bottom laser contacts. The load impedance of this circuit can be calculated as

$$Z_L = j\omega L + \frac{1}{1/R + j\omega C}, \quad (\text{A.1})$$

and the reflective amplitude is

$$\Gamma = \frac{Z_L - 50}{Z_L + 50} \quad (\text{A.2})$$

The capacitance is calculated from the geometry of the top and bottom contacts, and is estimated to be  $C \approx 0.05 \text{ pF}$ . The measured differential resistance of the small section above threshold is  $R = 30 \Omega$ . The small signal amplitude reflectance  $|\Gamma|$  of the laser circuit at 18 GHz was measured with a network analyzer to be approximately equal to 0.8. The inductance caused by the bonding wire can then be deduced from Eqs. (A.1) and (A.2) using the values of  $R$ ,  $C$ , and  $|\Gamma|$ . We obtain the inductance caused by the bonding wire to be approximately 1 nH, which agrees with that estimated elsewhere for a similar device [1]. We note that the reflective amplitude in our devices is rather insensitive to the capacitance, and is mainly determined by the inductance.

The current amplitude of the laser modulation is simulated numerically by the Runge-Kutta method using a short section I-V curve in Fig. 2 (black curve) and previously estimated  $C$  &  $L$  values. The simulated current amplitude vs. time across the laser is shown in Fig. 14 for 35 dBm of RF modulation power.

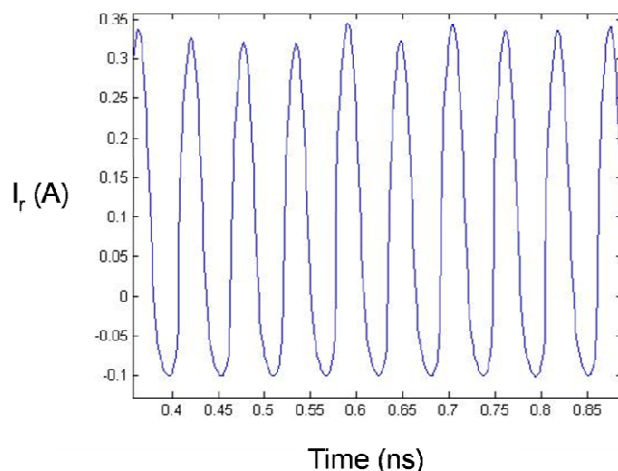


Fig. 14. Simulated current amplitude vs. time across the resistor.

In the negative direction, the current is clearly clamped due to the large differential resistance near zero voltage. The current amplitude swing is about 300mA in the positive direction and 100mA in the negative direction, resulting on average the amplitude of 200mA

Since the length of the bonding wire varies from device to device, the inductance may be different for each device. To see how much this change would affect the current modulation amplitude, we also simulated the cases  $L=2$  nH and  $0.5$  nH. For  $L=2$  nH, the average current amplitude is 140 mA, and for  $L=0.5$  nH, the average current amplitude becomes 250 mA. Note that a factor of two changes is an overestimation for the actual variation in  $L$ , thus the error in the estimated current amplitude across the laser should be no more than 25%. The capacitance, on the other hand, still has very little effect on the simulated current amplitude.

To convert the current modulation amplitude estimated above to the modulation amplitude  $m$  used in numerical simulations, we have to compare the amplitude of the current density modulation in a small section with the threshold current density of the device under DC pumping. For the  $16\mu\text{m}$  wide laser tested in the paper, the threshold current is 310mA. The modulation amplitude is then

$$m = \frac{200\text{mA}}{160\mu\text{m} \times 2} \bigg/ \frac{310\text{mA}}{2.6\text{mm}} \approx 5$$

where 200 mA is the simulated current amplitude,  $160 \mu\text{m}$  is the length of the short section, 310 mA is the threshold current, and 2.6 mm is the length of the whole cavity. The factor of two in the first denominator comes from the current spreading factor estimated previously. Thus, assuming  $L=1\text{nH}$ ,  $C=0.05$  pF, we estimate the modulation amplitude about 5 with 35dBm of applied RF power.

### Acknowledgments

The authors thank W. F. Andres for his help with the network analyzer and useful discussions as well as Ariel Gordon and Christian Jirauschek for initial implementations of the simulation tools used. They also thank D. Bour, S. Corzine and G. Höfler at Agilent Technologies for wafer growth. The Center for Nanoscale Systems (CNS) at Harvard University is also gratefully acknowledged. Harvard-CNS is a member of the National Nanotechnology Infrastructure Network (NNIN). This work was supported in part by the U.S. Army Research Laboratory and the U.S. Army Office under Grant No. W911NF-04-1-0253.